PAPER

Carbon-coated Si micrometer particles binding to reduced graphene oxide for a stable high-capacity lithium-ion battery anode†

Xiang Han,[a] Huixin Chen,[b] Ziqi Zhang,[a] Donglin Huang,[a] Jianfang Xu,[a] Cheng Li,[a] Songyan Chen*[a] and Yong Yang*[b]

Micrometer Si (MSi) particles are an attractive alternative as high energy-density lithium-ion battery anodes. To maintain the structural integrity and resolve the electrical conduction problem of MSi-based anodes, we propose novel MSi/C/reduced graphene oxide (RGO) through simple ball milling liquid polyacrylonitrile (PAN) with MSi and graphene oxide nanosheets, followed by thermal reduction. This structure capitalizes on the interaction of MSi and carbonized PAN with RGO sheets to provide a robust microarchitecture. The mechanical integrity of the *in situ* formed porous configuration can be dramatically improved by manipulating the size of unreacted Si nanocrystals. In addition, the Si–N–C layer serves as an electrolyte blocking layer, which helps to build a stable SEI layer and results in a high initial coulombic efficiency of 91.7%. Furthermore, the RGO binding to MSi/C acts as a flexible buffer during galvanostatic cycling, allowing microparticles to expand and fractured nanoparticles to anchor, while retaining electrical connectivity at both the particle and electrode levels. As a result, this hierarchical structure exhibits a superior reversible capacity of 1572 mA h g^{-1} with no capacity loss for 160 cycles at 0.2 A g^{-1} and over 628 mA h g^{-1} for 1000 cycles at 2 A g^{-1}.

1. Introduction

Silicon is at the forefront of applications in anode materials due to its 10 times higher lithium capacity than the current graphite material.[1–5] Micrometer-sized silicon (MSi) particles are a low-cost and high efficiency alternative but, unlike Si nanoparticles, they suffer from unavoidable particle fracture during electrochemical cycling.[6–11] Recently, Jaephil Cho and Soojin Park *et al.* used micro-sized bulk Si powder to produce multi-dimensional Si composed of porous nanowires and micro-sized cores by combining a metal deposition and chemical etching process.[12–14] Electrodes containing these materials achieved a high capacity within the first 50 cycles. Cui *et al.*[15] introduced a method to directly encapsulate Si microparticles (1–3 μm) using conformally synthesized cages of multilayered graphene. The graphene cage acts as a mechanically strong and flexible buffer and a stable SEI layer, thus achieving stable full cell cycling performance (100 cycles; 90% capacity retention).

In this work, to maintain the structural integrity and resolve the electrical conduction problem of MSi-based anodes, we propose novel MSi/C/reduced graphene oxide (RGO) through simple ball milling liquid polyacrylonitrile (PAN) with MSi and graphene oxide nanosheets, followed by thermal reduction. This structure capitalizes on the interaction of MSi and carbonized PAN with RGO sheets to provide a robust micro-architecture. The structural stability of the MSi powder electrode can be dramatically improved by manipulating the size of unreacted Si nanocrystals, which is differentiated from the existing methods that focus on controlling the morphology to withstand the lithiation/delithiation induced enormous mechanical stress. The lithiation of carbon-coated crystalline MSi shows an inhomogeneous process; uniform crystalline nano-Si seeds still remain after repeated cycles. In this sense, we control the Si nanocrystal size by precisely regulating the cut-off voltages; the remaining inactive crystalline Si seeds have diameters varying from ∼3 nm to 10 nm. Therefore the mechanical integrity drastically improved. In addition, our MSi/C composites exhibit high first coulombic efficiency (91.7%) at a low specific current of 0.2 A g^{-1} due to the compact Si–N–C interlayer. Furthermore, the long-life cycling stability of particle-based electrodes depends on the inter-particle electrical contact.

Our MSi/C anchored on the RGO composite explores an attractive alternative to traditional designs (binder and carbon-black), mainly due to flexible graphene binding to the MSi/C network with mechanical strength and ability to be

[a] Fujian Provincial Key Laboratory of Semiconductors and Applications, Collaborative Innovation Center for Optoelectronic Semiconductors and Efficient Devices, Department of Physics, Xiamen University, Xiamen 361005, P. R. China. E-mail: sychen@xmu.edu.cn

[b] State Key Laboratory for Physical Chemistry of Solid Surfaces, Department of Chemistry, Xiamen University, Xiamen 361005, P. R. China. E-mail: yyang@xmu.edu.cn

† Electronic supplementary information (ESI) available. See DOI: 10.1039/c6ta07274g

interconnected with fractured MSi particles. Large micrometer-sized RGO sheets could serve as support frames to MSi particles, providing the necessary electronic path and consistent cycling performance at high current densities along with high structural stability at the electrode level. Our material design resolves most rigorous drawbacks of Si anodes thus far, maintaining the electrical connectivity of fractured particles while simultaneously attaining high coulombic efficiencies. Consequently, this hierarchical structure presents a superior reversible capacity of 1572 mA h g^{-1} with no capacity loss for 160 cycles at 0.2 A g^{-1}.

2. Experimental

2.1 Materials synthesis

100 mg industrial photovoltaic silicon powders (99.99%, ~1.7 μm, Xuzhou Lingyun Silicon Industry Co., Ltd, China) were ball milled with a liquid PAN solution (1.1 g, 9 wt% dissolved in DMF) for 1.5 h at 500 rpm. The as-obtained slurry was spread onto copper foils with a diameter of 14 mm and dried for 1 h in a vacuum drying oven at 80 °C. Then the PAN-coated MSi electrodes were loaded into a tube furnace and heated to 700 °C for 6 h at a rate of 5 °C min^{-1} under Ar/H$_2$ (95% Ar and 5% H$_2$) protection. For the MSi/C/RGO electrode, 20 mg RGO powder was added into the above recipe. GO was prepared from natural graphite powder by the well-known modified Hummers method[16] as reported elsewhere.

2.2 Characterization

Scanning electron microscopy (SEM) (HITACHI S-4800) and transmission electron microscopy (TEM) (Philips Tecnai F30) were used to investigate the morphologies of the electrodes. Raman spectra were acquired using a WITEC Raman system with an excitation at λ = 488 nm. X-ray diffraction (XRD) patterns of the samples were obtained by using a Rigaku Ultima

IV with Cu Kα radiation. A Vario EL III (Elementar, Germany) was used to analyze the elemental content of the MSi/C composites. X-ray photoelectron spectroscopy (XPS) spectra were acquired with a PHI QUANTUM 2000 spectrometer. The active mass was carefully weighed by using a microbalance (METTLER TOLEDO XS3DU) with an accuracy of 1 μg.

2.3 Electrochemical testing

For electrochemical characterization, CR 2025 coin type half cells were fabricated in an Ar-filled box with MSi/C or MSi/C/RGO working electrodes and lithium foil counter electrodes. The total mass loading per electrode after annealing was 1.5–2 mg. The full cells contained MSi/C/RGO anodes and lithium cobalt oxide (LCO) cathodes with a mass ratio of 1 : 10. The LCO was mixed with carbon black (Super P) and the polyvinylidene fluoride (PVDF) binder (80 : 10 : 10 by weight) in N-methyl-2-pyrrolidinone to form a slurry. This slurry was then spread onto copper foils and dried under vacuum at 80 °C for 12 h to form the working electrode. The electrolyte used for all cells was 1 M LiPF$_6$ in ethylene carbonate (EC) dimethylcarbonate (DMC) and diethyl carbonate (DEC) (1 : 1 : 1 v/v) with 10% fluorinated ethylene carbonate (FEC) added. The galvanostatic cycling was performed between 0.005 V and 2.5 V at the temperature of 30 °C on a Land CT2001A system. Impedance spectroscopy from 100 kHz to 10 mHz under AC stimulus with an amplitude of 10 mV and no applied voltage bias was recorded using a four-channel multifunctional electrochemical workstation (VersaSTAT MC, America).

3. Results and discussion

Fig. 1a exhibits scanning electron microscopy (SEM) images of industrial photovoltaic silicon powders (99.99%) with an average size of ~1.7 μm and some non-uniform clippings found on the surface; the detailed size distribution is presented in
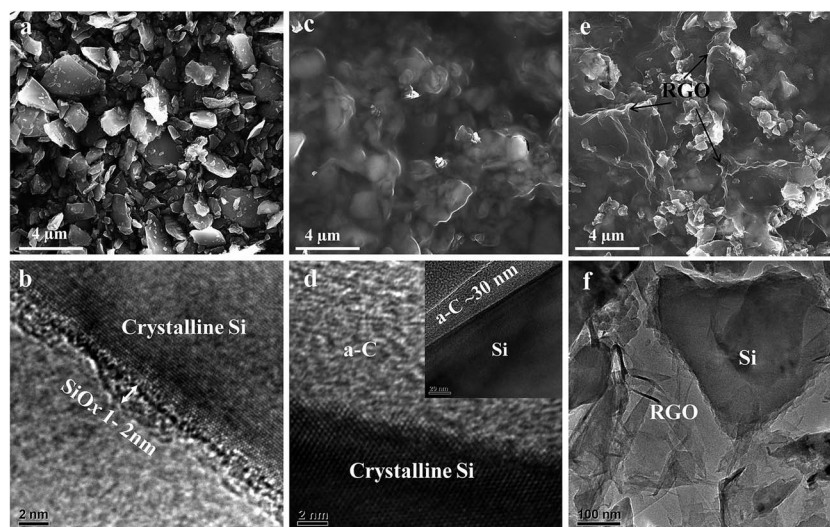

Fig. 1 (a) A SEM image of MSi particles. (b) A HRTEM image of a particular MSi particle. (c) A surface SEM image of MSi/C. (d) A high resolution TEM image of the MSi/C (inset is a low magnification TEM image of MSi/C). (e) A SEM image of the MSi/C/RGO surface. (f) A TEM image of MSi/C/RGO.

Fig. S1.† As shown in the high resolution transmission electron microscopy (HRTEM) image (Fig. 1b), a sparse native SiO_x layer with a thickness of 1–2 nm on the surface of the crystalline Si core with a plane spacing of 0.192 nm was observed. After annealing MSi/PAN in an Ar/H_2 atmosphere for 6 h at 700 °C, the silicon particles dispersed uniformly in the carbon network (Fig. 1c), which can serve as a mechanical support and provide a fast electron pathway. Fig. 1d presents an amorphous ∼30 nm carbon layer coated on the Si surface and no silicon oxide layer was observed on the as-received Si surface. Instead an amorphous carbon layer directly bonded with crystalline Si atoms, forming a compact interlayer, is observed. The fast Fourier transform (FFT) pattern (Fig. S2†) in Fig. 1d reveals that Si remains crystalline after annealing. However, the (111) plane spacing of MSi/C (0.316 nm) became larger than the standard plane spacing of Si (111) (0.314 nm), implying the presence of stress created by the difference in thermal expansion coefficients between Si and C.[4,17] Accordingly, the Si peaks in the X-ray diffraction (XRD) patterns (Fig. S3†) shifted to lower diffraction angles after annealing. For the MSi/C/RGO electrode, the MSi/C particles anchored on the 2D RGO layer with tens of micron scale (Fig. 1e). The wrinkled graphene sheets form a network around the MSi/C for securing good electrical connection between particles. To confirm the link between particles and graphene, transmission electron microscopy (TEM) analysis was conducted. The TEM image of MSi/C/RGO (Fig. 1f) shows MSi/C particles anchored on the large scale RGO network. The flexible RGO layers with wrinkle space between MSi particles are expected to accommodate the large volume change and to envelope the fractured particles.

Fig. 2a–c show the fine X-ray photoelectron spectroscopy (XPS) images of the MSi/C and MSi/C/RGO and the fitting spectra are shown in Fig. S4.† The C 1s spectra indicate that the fitting C=C peak shifts to a lower binding energy in MSi/C/RGO (284.7 eV) compared with MSi/C (285.0 eV) because of its higher degree of graphitization.[18] Both composites show peaks at 285.8 eV and 287.5 eV, suggesting that the bonding forming of doped nitrogen atoms correspond to sp^2-C and sp^3-C atoms, respectively.[19] The fitting N 1s high-resolution spectrum shows consistent results; the peaks are comprised of three components: pyridinic N, pyrrolic N and graphitic N.[20,21] Among these three styles of N binding, the pyridinic N is the most favorable for facilitating the electronic conductivity of the carbon layer and the charge transfer at the interface in Li-ion batteries. The ratio of pyridinic N to pyrrolic N increased from 1.9 to 2.2. The Si 2p high-resolution spectrum of both composites indicates the characteristic peak of Si (Si–Si, 99.9 eV).[22] In addition, a broad band at Si–N–C 102 eV that can be attributed to interfacial Si–N–C bonds confirms the strong interaction between Si and C. The Raman spectrum of MSi/C and MSi/C/RGO (Fig. 2d) reveals the highly graphitic nature of the RGO layers[15,23] as compared with amorphous carbon synthesized by pyrolysis of PAN. The 2D peak at *ca.* 2700 cm^{-1} is the characteristic peak of graphene, due to the two phonons with opposite momentum in the highest optical branch near the *K*-point, which can be used to distinguish graphene from other carbon materials in Raman spectra.[24] The above results demonstrate not only the homogenous dispersion of MSi in the composite material but also the strong interaction with the composite. This unique structure looks closely relevant to accommodate the deformation pressure from the $LiSi_x$ alloying/dealloying process to maintain its structural integrity and provide a fast electrical pathway for MSi.

Fig. 3a shows the cycling performance of the MSi/C at 0.2 A g^{-1} with different cut-off voltages. If not mentioned, all reported specific capacities are based on the total mass of MSi, a-C and RGO. For the MSi/C composites tested by elemental analysis, the contents of C, N and H were 20.7 wt%, 3.9 wt% and 0.7 wt% and Si was 74.7 wt% respectively. The MSi/C electrode delivered an initial discharge capacity of 2350 mA h g^{-1} with a high coulombic efficiency of 91.7%. The initial irreversible capacity loss can be mostly due to the initial SEI formation and the consumption of Li^+ by imperfect carbon (Fig. S5†). We attribute the high first-cycle efficiency to the low specific surface area of MSi/C and compact interfacial Si–N–C blocking layer. The typical galvanostatic charge/discharge profile of the MSi/C electrode of the first two cycles is shown in Fig. 3d, the observed plateau (∼80 mV) in the first charge curve represents alloying of crystalline Si with lithium.[8,25,26] For the 2nd cycle, it shows two typical lithiation/delithiation plateaus of a-Si.[27–29] However, the capacity fades quickly during the first 7 cycles due to large volume changes of crystalline Si during repeated lithiation and delithiation. However the capacity stabilizes around 2100 mA h g^{-1} after the hop point in the 8th cycle. Then, the capacity shows linear attenuation after 30 cycles with 1536 mA h g^{-1} retained after the 120th cycle. After 120 cycles, both the coulombic efficiency and capacity fade rapidly, and only hold 1080 mA h g^{-1} in the 157th cycle (46% retained). According to the capacity loss model of the Si anode proposed by C. P. Grey,[30] the decreasing lithiation capacity is primarily attributed to kinetics degradation after 120 cycles, the increased electrode tortuosity severely limiting Li^+
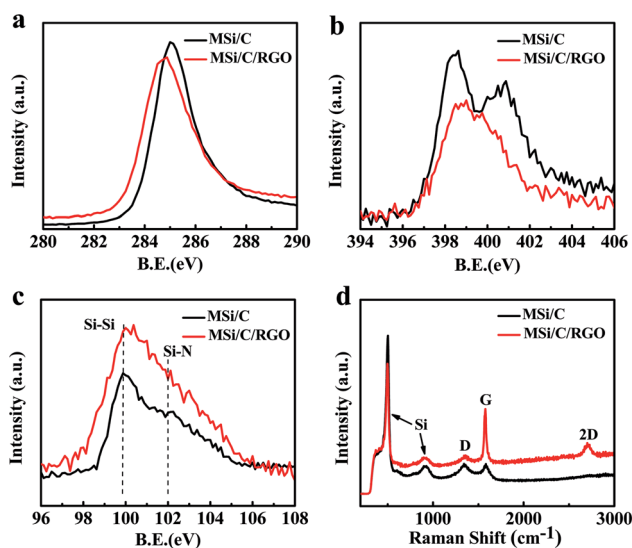
Fig. 2 XPS spectra of the MSi/C composite and MSi/C/RGO composite: (a) C 1s partial spectra of both composites, (b) N 1s partial spectra of both composites, and (c) Si 2p partial spectra of both composites. (d) Raman spectra of the MSi/C composite and MSi/C/RGO composite.
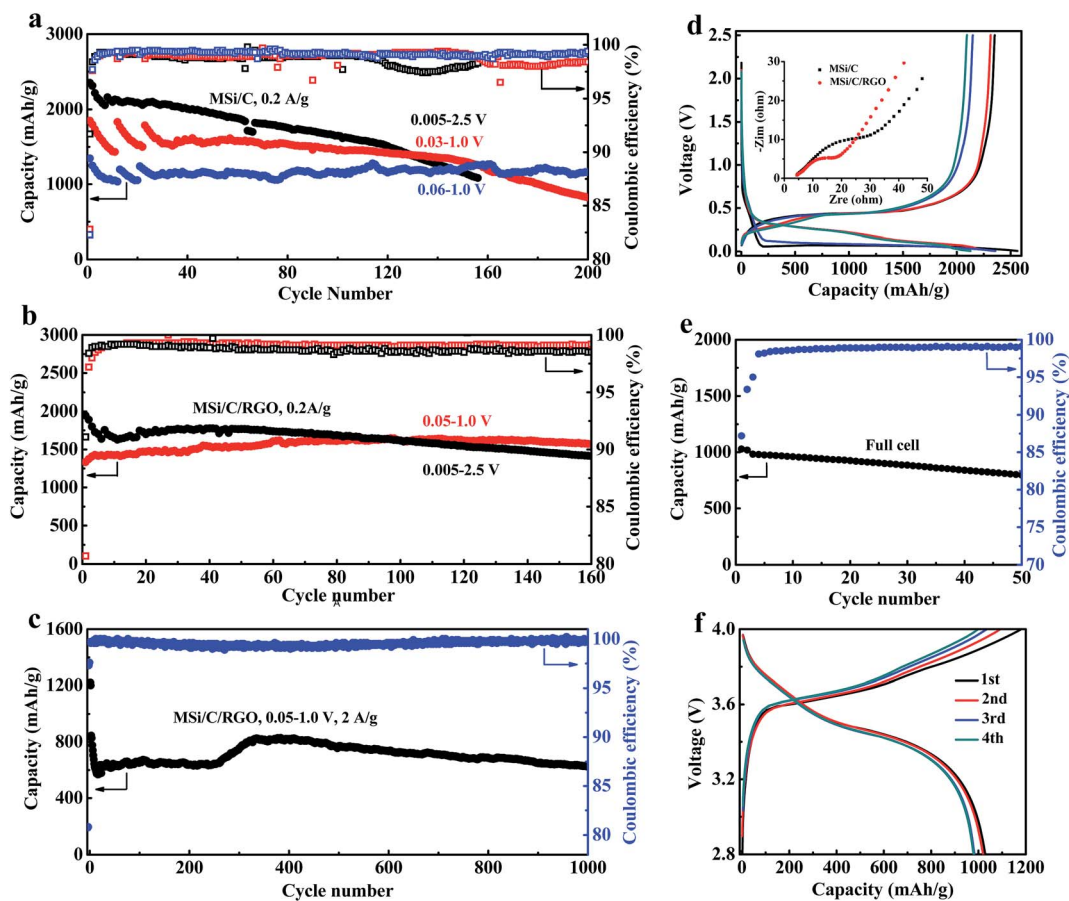
This journal is © The Royal Society of Chemistry 2016

J. Mater. Chem. A, 2016, **4**, 17757–17763 | **17759**

Fig. 3 (a) Half-cell delithiation capacity of MSi/C at a rate of 0.2 A g^{-1} between 0.005 and 2.5 V, 0.03–1.0 V, and 0.06–1.0 V. (b) Half-cell delithiation capacity of MSi/C/RGO at a rate of 0.2 A g^{-1} between 0.005 and 2.5 V and 0.05–1.0 V. (c) Half-cell delithiation capacity of MSi/C/RGO at a rate of 2 A g^{-1} between 0.05 and 1.0 V. (d) The first two voltage profiles of MSi/C and MSi/C/RGO at a rate of 0.2 A g^{-1} between 0.005 and 2.5 V; inset shows EIS measurements of MSi/C and MSi/C/RGO after the first two cycles at a rate of 0.2 A g^{-1} between 0.005 and 2.5 V (e) full-cell containing the LiCoO$_2$ cathode and MSi/C/RGO anode cycling between 2.8 and 4.0 V. (f) Voltage profiles of the full cells containing the LiCoO$_2$ cathode and MSi/C/RGO anode cycling between 2.8 and 4.0 V.

diffusion through the bulk of the electrode. In general, the increased electrode tortuosity is associated with degradation of mechanical integrity. Comparing the cycling performance with that of MSi/C cycling between 0.03 and 1.0 V and 0.06 and 1.0 V cut-off voltages, dramatic capacity decay was also observed during initial 10 cycles. However, improved capacity retention of 64% (1189 mA h g^{-1}) after 160 cycles was obtained despite a quick attenuation after 150 cycles between 0.03 and 1.0 V. In addition, the capacity retention of MSi/C was 94% (1267 mA h g^{-1}) after 160 cycles with a cutoff voltage of 0.06–1.0 V and no severe capacity decay was observed even after 200 cycles. Nonetheless, the average coulombic efficiencies improve from 98.9% to 99.3% while the cutoff voltage varies from 0.005–2.5 V to 0.06–1.0 V, which further confirmed that stable SEI and mechanical stability were obtained. Overall, cutoff voltage controlled MSi/C electrodes showed significantly improved cycling performances even though micrometer-sized Si particles without a structural design were used as anode materials.

The cycling stability of MSi/C composites was further enhanced by the designed RGO. As shown in Fig. 3b, the MSi/C/RGO electrode delivers an initial reversible capacity of

1947 mA h g^{-1} with 91.1% efficiency at 0.2 A g^{-1} between 0.005 and 2.5 V. It should be noted that the Si content here was only ∼65%. The impedance shows that the charge transfer resistance of the MSi/C electrode is larger than that of the MSi/C/RGO electrode (Fig. 3d), implying an improved electrical conductivity with RGO. In addition, the capacity retention of MSi/C/RGO after 157 cycles tested at 0.2 A g^{-1} between 0.005 and 2.5 V was 73% (1424 mA h g^{-1} retained), which is higher than that of MSi/C which is 46% (1083 mA h g^{-1} retained). Furthermore, no dramatic capacity decay was observed after ∼120 cycles despite a larger volume change of Si/C/RGO. We attribute the improved cycling stability to the enhanced electronic contact of the MSi/C particles binding to RGO layers. The synergistic effect of cut-off voltage control and improved electrical conductivity significantly enhanced the initial cycling stability, as shown in Fig. 3b, and no capacity decay of MSi/C/RGO was observed during the first 10 cycles. This may be because the flexible RGO was able to accommodate the volume change and to envelope the fractured pieces of MSi due to the strong interaction between MSi/C and graphene layers. Surprisingly, the cell containing MSi/C/RGO delivers a capacity

17760 | *J. Mater. Chem. A*, 2016, **4**, 17757–17763

This journal is © The Royal Society of Chemistry 2016

of 1572 mA h g^{-1} after 160 cycles at 0.2 A g^{-1} between 0.05 and 1.0 V. For the first time, no capacity loss was observed among micrometer-sized Si anodes during a low rate and long time testing period. To evaluate the synergistic effects of mechanical integrity control and improved electrical conductivity on high rate performance, the cycling stability of MSi/C/RGO was tested between 0.05 and 1.0 V at a rate of 2 A g^{-1} followed by initial two cycles at 0.2 A g^{-1} (Fig. 3c). The robust structure enables a very stable cycling, where a capacity of 626 mA h g^{-1} with 74% retention can be maintained for 1000 cycles. The capacity rising process during 250–350 cycles may be due to lithiation with the fractured porous powders anchored by the RGO layer. In addition to cycling stability, high coulombic efficiencies are critical for the operation of a practical battery. The MSi/C/RGO electrodes reached 99.9% after 10 cycles at 2 A g^{-1}. The high coulombic efficiencies can be explained in terms of MSi/C being mechanically stable to prevent additional SEI formation. The RGO layer maintains the electrical connectivity of the MSi/C anode at both the particle and the electrode level, while simultaneously reaching high coulombic efficiencies very rapidly.

A full cell paired with a lithium cobalt oxide (LCO) cathode was assembled to further investigate the MSi/C/RGO anode. The MSi/C/RGO anode exhibits a reversible capacity of 984 mA h g^{-1} at 1 A g^{-1} after stabilizing at 0.2 A g^{-1} for 2 cycles (Fig. 3e); the full cell retained a relative high capacity of 802 mA h g^{-1} after 50 cycles with an average working voltage of ~3.5 V (Fig. 3f). The fading mechanism of a Si-based full cell may be the consumption of the lithium available for cycling because of parasitic reactions and it is either trapped in an intermediate part of the SEI or in the electrolyte. At this point, without any available lithium left, the cell cannot function properly anymore.[31]

To reveal the fading mechanism of MSi/C during the long time cycling with various cut-off voltages, the morphology and inner crystalline structure of MSi/C electrodes after various cycles were investigated by TEM (Fig. 4). After 10 deep galvanostatic cycles between 0.005 and 2.5 V, the MSi/C electrode *in situ* formed an integrated porous configuration and the pores may be caused by repeated deformation pressure from the LiSi$_x$ alloying/dealloying process. The same phenomenon was also observed in Ge nanowires.[32] In the HRTEM image, Si nanocrystals with a diameter of ~3 nm could be found surrounded by an amorphous framework, revealing the amorphization of crystalline MSi embedded with crystalline Si nanodomains.[33] Therefore, the cycling stability improved during 10–30 cycles due to the formation of this unique configuration. Even after 100 cycles (Fig. S4†), the porous integrated framework still existed and the Si nanocrystals were found with the same distribution and diameter as those of the 9th cycle. Unfortunately, the mechanical integration of the porous configuration faded gradually during 120–157 cycles, and the electrodes presented separated porous Si/C pieces with a scale of ~150 nm (Fig. 4b), which may be caused by repeated huge deformation stress. In previous studies, nano-Si particles with a diameter <150 nm could withstand the huge stress without self-structure fracture.[34,35] The remaining Si nanocrystals with a diameter of ~3 nm were not able to maintain the mechanical stability during a long life cycling. The mechanical integration degeneration induces two serious challenges to overcome: (1) the increased electrode tortuosity severely limiting Li$^+$ diffusion through the bulk of the electrode; (2) new solid electrolyte chemical reactions on the surface of the small fractured pieces, which caused low coulombic efficiency and consumption of the electrolyte. Therefore, the cycling performance faded quickly.

Controlling the cut-off voltage was able to improve the mechanical integrity of the *in situ* formed porous powder. Fig. 4c shows the TEM images of the MSi/C electrode after 10 cycles tested at 0.2 A g^{-1} between 0.06 and 1.0 V; as expected, a large portion of the remaining crystalline Si was observed after 10 cycles. The crystalline nature of the inactive blocks with
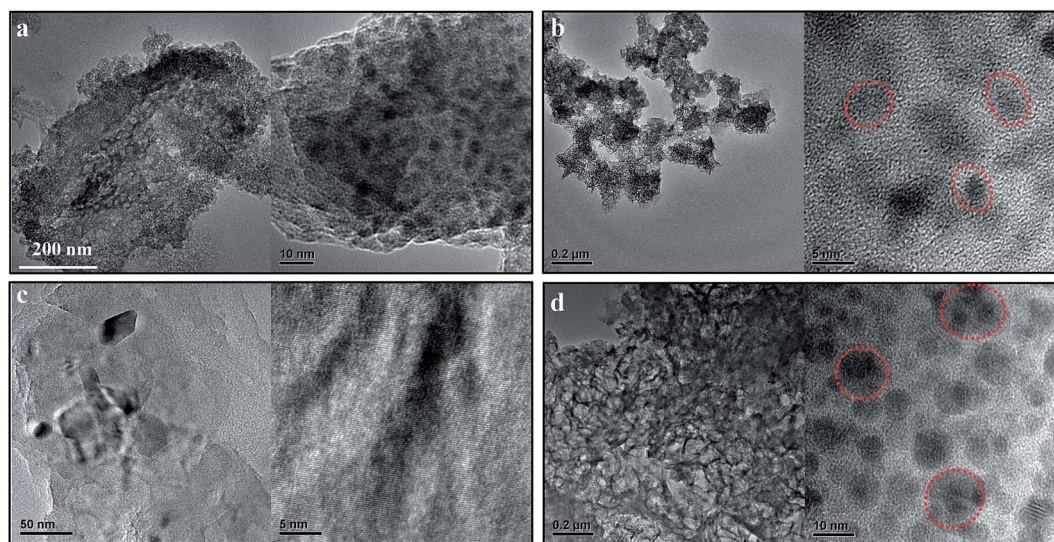

Fig. 4 Morphology and crystalline structure evolution of MSi/C electrodes at a rate of 0.2 A g^{-1} with different cut-off voltages: (a) 9 cycles between 0.005 and 2.5 V, (b) 157 cycles between 0.005 and 2.5 V, (c) 10 cycles between 0.06 and 1.0 V, and (d) 220 cycles between 0.06 and 1.0 V.
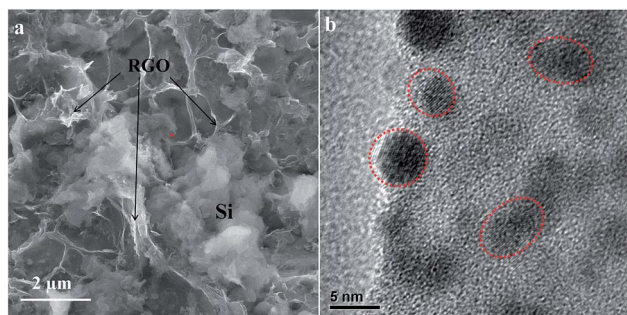
Fig. 5   (a) SEM image of the MSi/C/RGO surface after 1000 cycles at 2 A g^{-1} between 0.05 and 1.0 V. (b) HRTEM image of the MSi/C/RGO surface after 1000 cycles at 2 A g^{-1} between 0.05 and 1.0 V.

a scale of 30–50 nm was confirmed by the HRTEM image of Fig. 4c. The core–shell lithiation mechanism of crystalline Si was observed in previous studies.[36,37] It is clear that the crystalline structure evolution of MSi/C is controlled by manipulating cutoff voltages. Nonetheless, even after 220 cycles (Fig. 4d) the MSi/C electrode between 0.06 and 1.0 V still presented an interconnected porous structure with embedded uniform nano-Si crystals (8–10 nm). The larger portion and size of Si nanocrystals imply smaller deformation stress at the surface of MSi,[38] which is beneficial to hold the mechanical integrity of the porous configuration powders and the whole electrode.

To confirm the synergistic effect of crystalline structure evolution control and improved electrical conductivity on the cycling performance, the coin half cell containing MSi/C/RGO cycled between 0.05 and 1.0 V at 2 A g^{-1} was disassembled after 1000 cycles. As shown in Fig. 5a, the micron-meter Si particle converted to an interconnected porous configuration due to the repeated expansion and shrinkage during cycling. Moreover, Si nanocrystals with a controlled size of ∼5 nm were observed (Fig. 5b), which could act as supporting dots to hold the mechanical integrity on a particle scale. Furthermore, the flexible RGO layer with wrinkles was able to accommodate the large volume change within 1000 cycles. Consequently, the RGO acts as a 3D conducting network anchoring the *in situ* formed porous powders while holding the electrical integrated contact of the whole electrode. It is clear that designing the microarchitecture of the electrode by controlling crystalline structure evolution and by designing the RGO framework prevent fracture and electrical contact loss of MSi/C, maintaining reversible cycle stability for 1000 cycles.

4.   Conclusion

In conclusion, we present new design principles and opportunities of high-capacity Si anodes at a micro-scale for next-generation energy storage systems. Generally, combining a simple and scalable method, a robust microarchitecture of the MSi/C/RGO anode was fabricated. The structural stability of the micrometer-sized silicon powder electrode can be dramatically improved by manipulating the crystalline structure evolution. Moreover, the inactive Si–N–C interlayer serves as the electrolyte

blocking layer and helps to build a stable SEI layer. Furthermore, the RGO binding to MSi/C acts as a mechanically strong and flexible buffer during galvanostatic cycling, allowing the microparticles to expand and fractured nanoparticles to anchor while retaining electrical connectivity at both the particle and the electrode level. As a result, two long-standing issues with microscale Si have been resolved: particle fracture and SEI stability. Our work should motivate research into the crystal structure evolution and manipulation that governs the cycling stability of high-capacity alloying electrodes, which could be used to build high-performance lithium-ion batteries.

Acknowledgements

References

1 M. Armand and J. M. Tarascon, *Nature*, 2008, **451**, 652.

2 A. Magasinski, P. Dixon, B. Hertzberg, A. Kvit, J. Ayala and G. Yushin, *Nat. Mater.*, 2010, **9**, 353.

3 N. Liu, Z. Lu, J. Zhao, M. T. McDowell, H. W. Lee, W. Zhao and Y. Cui, *Nat. Nanotechnol.*, 2014, **9**, 187.

4 F. M. Hassan, V. Chabot, A. R. Elsayed, X. C. Xiao and Z. W. Chen, *Nano Lett.*, 2014, **14**, 277.

5 B. Wang, T. Qiu, X. Li, B. Luo, L. Hao, Y. Zhang and L. Zhi, *J. Mater. Chem. A*, 2015, **3**, 494.

6 H. Wu, G. Chan, J. W. Choi, I. Ryu, Y. Yao, M. T. McDowell, S. W. Lee, A. Jackson, Y. Yang, L. B. Hu and Y. Cui, *Nat. Nanotechnol.*, 2012, **7**, 309.

7 H. Wu and Y. Cui, *Nano Today*, 2012, **7**, 414.

8 C. K. Chan, H. Peng, G. Liu, K. Mcilwrath, X. F. Zhang, R. A. Huggins and Y. Cui, *Nat. Nanotechnol.*, 2008, **3**, 31.

9 H. Wu, G. Chan, J. W. Choi, I. Ryu, Y. Yao, M. T. McDowell and Y. Cui, *Nat. Nanotechnol.*, 2012, **7**, 310.

10 H. Chen, Y. Xiao, L. Wang and Y. Yang, *J. Power Sources*, 2011, **196**, 6657.

11 X. Huang, J. Yang, S. Mao, J. Chang, P. B. Hallac, C. R. Fell and J. Chen, *Adv. Mater.*, 2014, **26**, 4326.

12 B. M. Bang, H. Kim, H. K. Song, J. Cho and S. Park, *Energy Environ. Sci.*, 2011, **4**, 5013.

13 S. Sim, P. Oh, S. Park and J. Cho, *Adv. Mater.*, 2013, **25**, 4498.

14 B. M. Bang, J. I. Lee, H. Kim, J. Cho and S. Park, *Adv. Energy Mater.*, 2012, **2**, 878.

15 Y. Li, K. Yan, H. W. Lee, Z. Lu, N. Liu and Y. Cui, *Nat. Energy*, 2016, **1**, 15029.

16 W. S. Hummers Jr and R. E. Offeman, *J. Am. Chem. Soc.*, 1985, **80**, 1339.

17 D. Nesheva, C. Raptis, A. Perakis, I. Bineva, Z. Aneva, Z. Levi and H. Hofmeister, *J. Appl. Phys.*, 2002, **92**, 4678.

18 L. Q. Xu, W. J. Yang, K. G. Neoh, E. T. Kang and G. D. Fu, *Macromolecules*, 2010, **43**, 8336.

17762 | *J. Mater. Chem. A*, 2016, **4**, 17757–17763

This journal is © The Royal Society of Chemistry 2016

19 M. Thakur, R. B. Pernites, N. Nitta, M. Isaacson, S. L. Sinsabaugh, M. S. Wong and S. L. Biswal, *Chem. Mater.*, 2012, **24**, 2998.

20 D. M. Piper, T. A. Yersak, S. B. Son, S. C. Kim, C. S. Kang, K. H. Oh and S. H. Lee, *Adv. Energy Mater.*, 2013, **3**, 697.

21 Z. H. Sheng, L. Shao, J. J. Chen, W. J. Bao, F. B. Wang and X. H. Xia, *ACS Nano*, 2011, **5**, 4350.

22 C. F. Sun, H. Zhu, M. Okada, K. J. Gaskell, Y. Inoue, L. Hu and Y. Wang, *Nano Lett.*, 2015, **15**, 703.

23 F. M. Hassan, R. Batmaz, J. Li, X. Wang, X. Xiao, A. Yu and Z. Chen, *Nat. Commun.*, 2015, **6**, 8597.

24 A. C. Ferrari, J. C. Meyer, V. Scardaci, C. Casiraghi, M. Lazzeri, F. Mauri, S. Piscanec, D. Jiang, K. S. Novoselov, S. Roth and A. K. Geim, *Phys. Rev. Lett.*, 2006, **97**, 187401.

25 H. Li, X. Huang, L. Chen, G. Zhou, Z. Zhang, D. Yu and N. Pei, *Solid State Ionics*, 2000, **135**, 181.

26 Y. S. Hu, R. Demir-Cakan, M. M. Titirici, J. O. Muller, R. Schlogl, M. Antonietti and J. Maier, *Angew. Chem., Int. Ed.*, 2008, **47**, 1645.

27 J. Saint, M. Morcrette, D. Larcher, L. Laffont, S. Beattie, J. P. Peres, D. Talaga, M. Couzi and J. M. Tarascon, *Adv. Funct. Mater.*, 2007, **17**, 1765.

28 H. T. Nguyen, M. R. Zamfir, L. D. Duong, Y. H. Lee, P. Bondavalli and D. Pribat, *J. Mater. Chem.*, 2012, **22**, 24618.

29 X. Han, H. Chen, X. Li, J. Wang, C. Li, S. Chen and Y. Yang, *J. Mater. Chem. A*, 2016, **4**, 434.

30 A. L. Michan, G. Divitini, A. J. Pell, M. Leskes, C. Ducati and C. P. Grey, *J. Am. Chem. Soc.*, 2016, **138**, 7918.

31 N. Dupré, P. Moreau, E. De Vito, L. Quazuguel, M. Boniface, A. Bordes and D. Guyomard, *Chem. Mater.*, 2016, **28**, 2577.

32 T. Kennedy, E. Mullane, H. Geaney, M. Osiak, C. O'Dwyer and K. M. Ryan, *Nano Lett.*, 2014, **14**, 716.

33 Y. He, L. Zhong, F. Fan, C. Wang, T. Zhu and S. X. Mao, *Nat. Nanotechnol.*, 2016, **11**, 866.

34 X. H. Liu, L. Zhong, S. Huang, S. X. Mao, T. Zhu and J. Y. Huang, *ACS Nano*, 2012, **6**, 1522.

35 M. T. McDowell, S. W. Lee, W. D. Nix and Y. Cui, *Adv. Mater.*, 2013, **25**, 4966.

36 X. H. Liu, F. Fan, H. Yang, S. Zhang, J. Y. Huang and T. Zhu, *ACS Nano*, 2013, **7**, 1495.

37 A. Bordes, E. De Vito, C. Haon, A. Boulineau, A. Montani and P. Marcus, *Chem. Mater.*, 2016, **26**, 1566.

38 L. Luo, H. Yang, P. Yan, J. J. Travis, Y. Lee, N. Liu and J. G. Zhang, *ACS Nano*, 2015, **9**, 5559.